Comparison of Cu and Pt point-contact electrodes on proton conducting $BaZr_{0.7}Ce_{0.2}Y_{0.1}O_{3-\delta}$

Shay Robinson[a], Christian Kjølseth[b], Truls Norby[a]

[a] *Centre for Materials Science and Nanotechnology, Department of Chemistry, University of Oslo, FERMiO, Gaustadalléen 21, NO-0349 Oslo, Norway*
[b] *CoorsTek Membrane Sciences AS, Gaustadalléen 21, NO-0349 Oslo, Norway*

Abstract

The hydrogen oxidation kinetics of Cu and Pt point contact-electrodes on proton conducting $BaZr_{0.7}Ce_{0.2}Y_{0.1}O_{3-\delta}$ (BZCY72) were studied over a range of temperatures and hydrogen pressures using impedance spectroscopy. Characteristic capacitances were used to identify process contributions as charge and mass transfer, then Langmuir adsorption theory and Butler-Volmer charge transfer formalism were used to propose a hydrogen oxidation model to describe the experimental data. The charge transfer hydrogen pressure dependencies were $pH_2^{3/4}$ for Cu, attributed to a high occupancy of adsorbed oxygen at three-phase boundary sites in the water-vapor containing atmosphere, and $pH_2^{-1/4}$ for Pt, corresponding to a hydrogen saturated interface. The Cu and Pt point contact electrodes exhibit similar temperature dependencies for charge transfer, with activation enthalpies of 0.82 and 0.93 eV, and pre-exponentials of approximately 160 and 1000 $\Omega^{-1}cm^{-1}$, respectively. Mass transfer dominated the total polarization resistance of both metal point contact electrodes, exhibiting a $pH_2^{1/2}$ hydrogen pressure dependency. The activation enthalpies are $1.21\,eV$ for Cu and $0.73\,eV$ for Pt, reflecting the higher catalytic activity generally expected for Pt. Pre-exponentials for mass transfer of approximately 10000 $\Omega^{-1}cm^{-1}$ for Cu and 2.6 $\Omega^{-1}cm^{-1}$ for Pt, indicate that Cu utilizes a much larger active interface. Cu may be a suitable candidate electrode material for use in carbonaceous atmospheres, but the results of this work indicates that it suffers from a high activation enthalpy for mass transfer in the hydrogen oxidation reaction.

Keywords: Point-contact electrode, Hydrogen oxidation, Platinum, Copper, Proton ceramic

1. Introduction

1.1. Background

The bulk properties, stability and performance of many different ABO_3 perovskite proton conductors, such as $BaZr_{0.9-x}Ce_xY_{0.1}O_{3-\delta}$ (BZCY), have been extensively investigated for more than three decades [1–15]. However, mixed ionic-electronic conducting electrodes that are suitable for hydrocarbon utilization in BZCY electrochemical devices have not been reported. Such electrodes are subject to a number of constraints. First, the electrode must be chemically and mechanically compatible with the carbonaceous gas phase, the electrolyte, and the interconnects. This emphasizes a resistance to carbon deposition, which would reduce the number of three-phase boundary (3pb) sites and subsequently deactivate the electrode. Both Cu and BZCY exhibit a resistance to carbon deposition [16–20], and this makes these materials attractive for the development of industrial applications with hydrocarbons using proton ceramics. Second, it is also desirable that the electrode provides catalytic activity towards the hydrogen oxidation reaction (HOR) at the anode of any electrochemical device. Many researchers have studied Cu as a suitable metal for application as an electrode in solid oxide fuel cells, and though Cu is an excellent electronic conductor, it suffers from poor HOR kinetics due to a lack of catalytic activity [21–24]. Thus, better characterization and understanding of the HOR kinetics at the Cu-BZCY interface is necessary in order to develop an electrode suitable for applications such as fuel cells and membrane reactors in carbon containing atmospheres.

1.2. Approach

In this work, metal point-contact electrodes were used to directly compare the HOR kinetics of Cu and Pt at the metal-BZCY72 (x = 0.2) electrolyte interface. Pt is well researched, and known to have good catalytic activity towards the HOR [25, 26]; thus it is a valuable metal with which to compare the kinetic behavior of Cu. An HOR model, based on Langmuir adsorption theory and Butler-Volmer charge transfer formalism, is proposed to interpret experimental data obtained through electrochemical impedance spectroscopy (EIS). The HOR model was used to identify and explain hydrogen pressure (pH_2) dependencies, and temperature dependencies were used to extract activation enthalpies and pre-exponentials in order to compare the reaction kinetics of the two metals.

1.3. Point-contact electrode architecture

Point-contact electrodes are useful configurations with which to obtain detailed information about the reaction kinetics at the metal-electrolyte interface. The simple geometry of point-contact electrodes removes variables such as porosity and microstructure, and simplifies the complexities of composite electrodes, significantly reducing the length of the 3pb. Newman's formula, (1), has been used by numerous researchers in similar point-contact electrode studies [27–33].

$$r = \frac{1}{4\,\sigma_k\,R_j} \tag{1}$$

The calculation yields the radius (r) of the point-contact electrode area (assumed to be circular) and is inversely proportional to the measured electrolyte resistance (R_j) and known electrolyte conductivity (σ_k). For point-contact electrode configurations, the 3pb is restricted to the perimeter of the contact area of the metal-electrolyte interface.

1.4. Hydrogen oxidation reaction pathways

Fig. 1 schematically depicts the metal point-contact electrode to electrolyte interface and suggests potential reaction paths, which may progress in multiple steps and possibly through competing mechanisms. The proposed

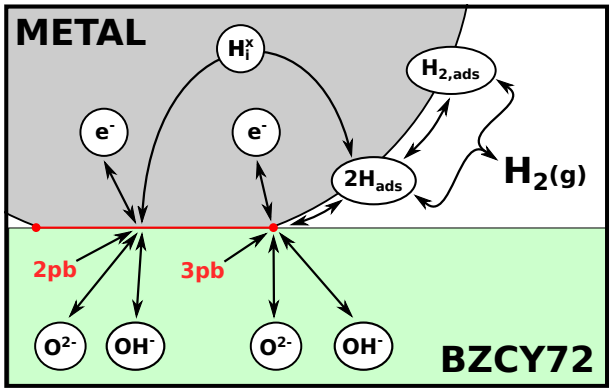

Figure 1: Possible reaction paths at the point-contact metal-BZCY72 interface: Associative ($H_{2,ads}$) and dissociative adsorption ($2H_{ads}$), with surface diffusion to the 3pb or interstitial diffusion (H_i^x) to the 2pb, and finally proton transfer to an oxide ion (O^{2-}).

reaction paths first involve the adsorption of H_2 onto the metal electrode

surface. This can occur associatively, leading to the physisorption of molecular hydrogen, $H_{2,ads}$. Associatively physisorbed species must then overcome an additional energy barrier in order to dissociate and become chemisorbed atomic hydrogen, H_{ads} [26, 34–36]. Dissociative adsorption of hydrogen is favorable on Pt surfaces due to the catalytic activity of the metal, leading directly to atomic chemisorbed H_{ads}. Then there are then two possible paths H_{ads} may take before the charge transfer step. H_{ads} may diffuse on the metal surface to the 3pb, where charge transfer then takes place. Or, after dissociation neutral hydrogen may dissolve interstitially as H_i^x and diffuse through the Cu metal to the two-phase boundary (2pb) of the metal-electrolyte interface. Hydrogen permeability in Cu is non-negligible, and has been reported at temperatures as low as 325 °C [37–40]. Thus, depending upon operating conditions and upon the electrode material employed, hydrogen may potentially be incorporated into the electrolyte via both mechanisms.

2. Experimental

2.1. Methods and materials

Electrolyte pellets were prepared from spray pyrolyzed BZCY72 nanopowder (CerPoTech) containing 1 wt.% ZnO (Sigma Aldrich). ZnO has been shown to be an effective sintering aid to achieve uniform grain growth and high density in BZY [41, 42]. The powders were ball milled in a yttrium stabilized zirconia (YSZ) jar with isopropyl alcohol, and then hand mixed with 1 wt.% PVB (Sigma Aldrich) binder. After drying overnight at 120 °C, the powder was uniaxially cold pressed into discs at 500 MPa, and sintered at 1500 °C for 10 hours. The sintered pellets were approximately 95% of the theoretical density of BZCY72 [43].

One side of the sintered disc was polished to a high finish for the point contact electrode interface, and the other side was polished moderately to facilitate adhesion of the Pt counter electrode. Pt ink was applied to two concentric regions, as shown in Fig. 2, to serve as the counter and reference electrodes, and then fired at 1100 °C for two hours. A point-contact electrode assembly was constructed by wrapping 0.5 mm Pt wire (Thermocouple quality, K.A. Rasmussen, Hamar, Norway) or 0.5 mm Cu wire (Alfa Aesar #10973, 99.999%) around small diameter alumina tube. The point electrode assembly was then secured on the top of the polished surface of the electrolyte with spring loaded alumina rods. A second identical sintered disc

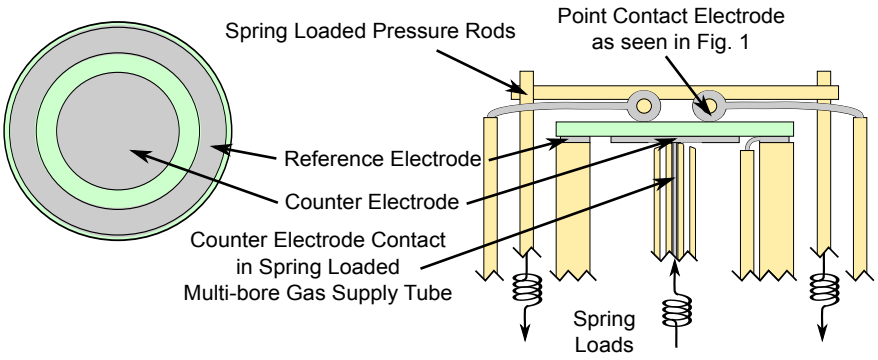

Figure 2: Point contact electrode schematic.

was also prepared for a standard conductivity measurements. Symmetric Pt electrodes of ~0.8 cm diameter were painted on each side of the second pellet, corresponding to the counter electrode in Fig. 2.

2.2. Procedure

EIS measurements were conducted every 25 °C while decreasing the temperature from 600 to 450 °C. Hydrogen and water vapor pressures were changed systematically; pH_2 was tested at 0.5, 0.05, and 0.005 atm., for each pH_2O of 0.027 and 0.0027 atm. Once reaching equilibrium, as determined by a 10 kHz impedance measurement, frequency sweeps were performed in the range 1 MHz to 10 mHz with a 50 mV AC amplitude, using a Gamry REF-3000.

EIS measurements were also performed on the symmetric Pt electrode pellet in order to obtain the electrolyte conductivity, σ_k, for use in Newman's formula. The impedance measurements were taken from 600 °C to 150 °C in a $pH_2 = 0.05$ / $pH_2O = 0.027$ atmosphere. All impedance spectra deconvolutions were done using the analysis software Z-View.

3. Results

3.1. Point-contact electrode-electrolyte interface

Using the electrolyte conductivity, σ_k, in combination with the measured electrolyte resistance, R_j, for the Cu and Pt point electrodes, the radius of the contact area of each electrode was calculated with (1). The activation energy at the lowest temperatures, obtained from the regression of $\ln(\sigma T)$ vs.

$1/T$, was calculated to be $E_a = 0.48\,eV$, which is in agreement with literature [41, 44] for the proton conductivity of BZCY materials. The mean values of the radii were $r_{Cu} \cong 0.027\ cm$ and $r_{Pt} \cong 0.028\ cm$, yielding contact areas of $A_{Cu} \cong 0.0026\ cm^2$ and $A_{Pt} \cong 0.0033\ cm^2$, and perimeters of $P_{Cu} \cong 0.17\ cm$ and $P_{Pt} \cong 0.18\ cm$, for the Cu and Pt point electrodes, respectively. SEM images of the Pt and Cu point-contact electrode-electrolyte interfaces are shown in Fig. 3.

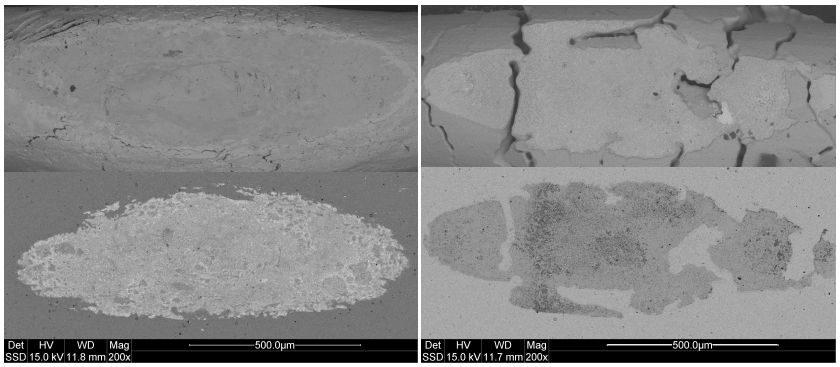

Figure 3: Post testing SEM images of the Pt (ℓ) and Cu (r) point-contact electrode to electrolyte interfaces, showing the metal electrodes (*top*) and the electrolyte (*bottom*) surface. Images have been enhanced to show the contrast of the interface.

The detailed perimeters of each of the point contact electrodes, seen in Fig. 3, were traced using graphics software. A correlation with the scale bars in the SEM images was established and used to estimate the length of each perimeter, yielding 0.58 cm for the Cu point contact and 0.50 cm for the Pt point contact. The software also estimated each of the contact areas as 0.0028 and 0.0032 cm^2 for Cu and Pt, respectively. Based on the correlation between the calculated and estimated contact areas, the software generated perimeters are considered to be better estimates of each of the point-contact 3pb lengths than those obtained with (1) due to the irregular perimeter of the actual contact area, as seen in Fig. 3.

3.2. Representative impedance spectra and data analysis

Representative impedance spectra are shown in Fig. 4, and are composed of multiple overlapping arcs.

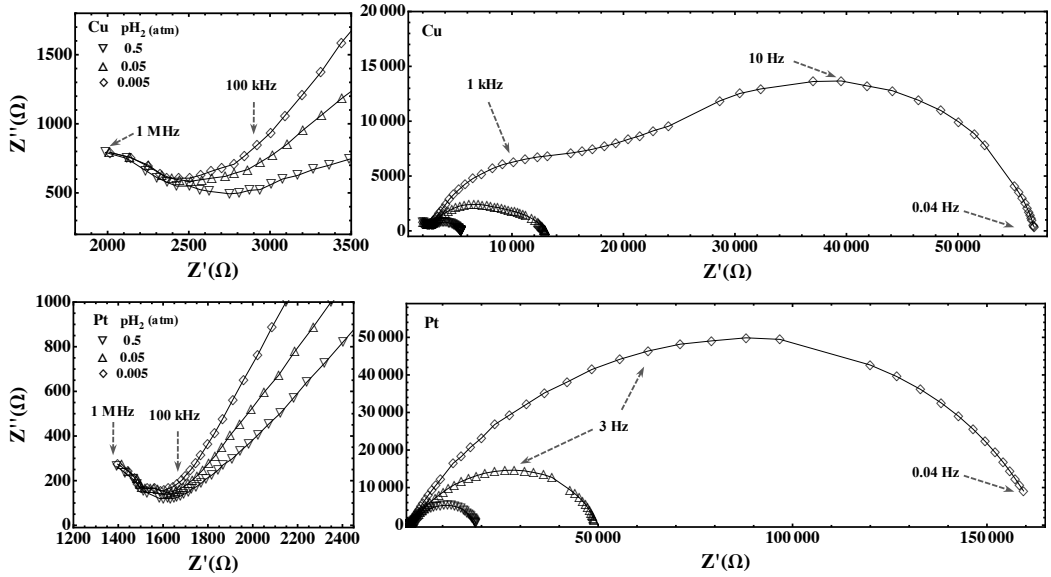

Figure 4: Representative impedance spectra (noise removed) for the Cu (*top*), and Pt (*bottom*) point electrodes, showing high (*left*) and low (*right*) frequency components. Spectra were obtained at 600°C by varying pH_2 in a pH_2O = 0.0027 atm.

Spectra deconvolutions were performed in the software Zview using an equivalent circuit composed of a resistor, a series of parallel resistor and constant phase element (R-QPE) components, and a Gerischer element, as shown in Fig. 5. The Gerischer element was used due to the asymmetric shape of the low frequency response, and was applied only once higher frequency parameters had been fixed.

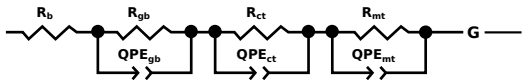

Figure 5: R-QPE equivalent circuit used in the deconvolution of point-contact electrode and electrolyte conductivity data

Point-contact electrodes exhibit capacitances that are much smaller than those typically observed for disk samples, however, it is the difference in magnitude of each characteristic that allows it to be assigned to a specific process [45, 46]. In Fig. 4, the arcs at the high frequency response near 1 MHz have

calculated *area specific* QPE capacitances in the order of $10^{-11} F\, cm^{-2}$; thus these contributions were attributed to electrolyte grain boundary resistance, R_{gb}. The higher frequency intercept of each grain boundary arc (not seen) was attributed to electrolyte bulk resistance, R_b. The grain boundary, R_{gb}, and bulk, R_b, resistances were summed into an electrolyte volume resistance, R_v.

The intermediate frequency response is commonly attributed to charge transfer, and in the Cu point-contact electrode spectra shown in Fig. 4 (*top*), is apparent from approximately 100 kHz to 500 Hz. This same frequency range in the Pt point-contact electrode spectra, Fig. 4 (*bottom*), is barely visible in comparison. The lowest frequency arc was attributed to electrode mass transfer processes. The sum of the low frequency R-QPE resistance and the Gerischer contribution was attributed to mass transfer, and defined as R_{mt}.

Raw capacitance values for charge transfer and mass transfer, that are seen in Fig. 6, are of the order $10^{-8} F$ and $10^{-7} F$ for Cu, and $10^{-7} F$ and $10^{-6} F$ for Pt. The above values are independent of temperature and subject to assumptions of a dominant process path: charge transfer can be subject to 2pb contact area (cm^{-2}) or 3pb length (cm^{-1}) specificity, while mass transfer can be based on 2pb contact area, 3pb length or electrode volume (cm^{-3}) specificity. Table 1 reports these values, as outlined above, by taking the mean values with hydrogen and water vapor pressure, as seen in Fig. 6, and the lengths and areas reported in the previous section. The electrode volume was calculated using the wire diameter as length, yielding 3.9 $\times 10^{-4}$ cm^3.

Table 1: The mean unspecific capacitance, with tpb length, contact area and volume specificity.

Process specificity	Cu (F)	Pt (F)
ct unspecific	9.6×10^{-9}	4.7×10^{-8}
ct (cm^{-1})	5.6×10^{-9}	2.4×10^{-8}
ct (cm^{-2})	2.7×10^{-11}	1.5×10^{-10}
mt unspecific	2.1×10^{-7}	1.5×10^{-6}
mt (cm^{-1})	1.2×10^{-7}	7.5×10^{-7}
mt (cm^{-2})	5.9×10^{-10}	4.8×10^{-9}
mt (cm^{-3})	8.2×10^{-11}	5.9×10^{-10}

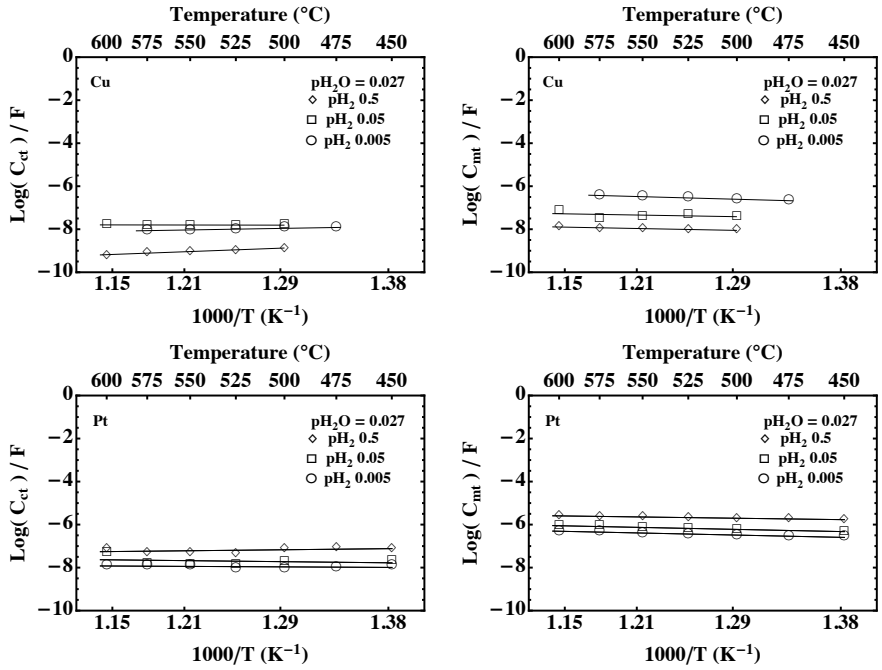

Figure 6: Three phase boundary length specific capacitances for charge transfer (*left*) and mass transfer (*right*) for both Cu (*top*) and Pt (*bottom*) at pH_2O = 0.027 atm.

In the following sections capacitances are presented in terms of unspecific raw values, while charge and mass transfer conductances are treated using 3pb length specific assumptions.

3.3. pH_2 dependencies

Deconvolutions of the impedance spectra data were plotted as $\mathrm{Log}(1/R_i)$ vs. pH_2, and are shown in Fig. 7. The average slope is shown at the bottom of each plot for electrolyte volume, charge and mass transfer at pH_2O = 0.027 atm. and pH_2O = 0.0027 atm. For both the Cu and Pt point-contact electrodes, the electrolyte conductance $1/R_v$, is observed to be nearly pH_2 independent, as expected for the BZCY72 electrolyte.

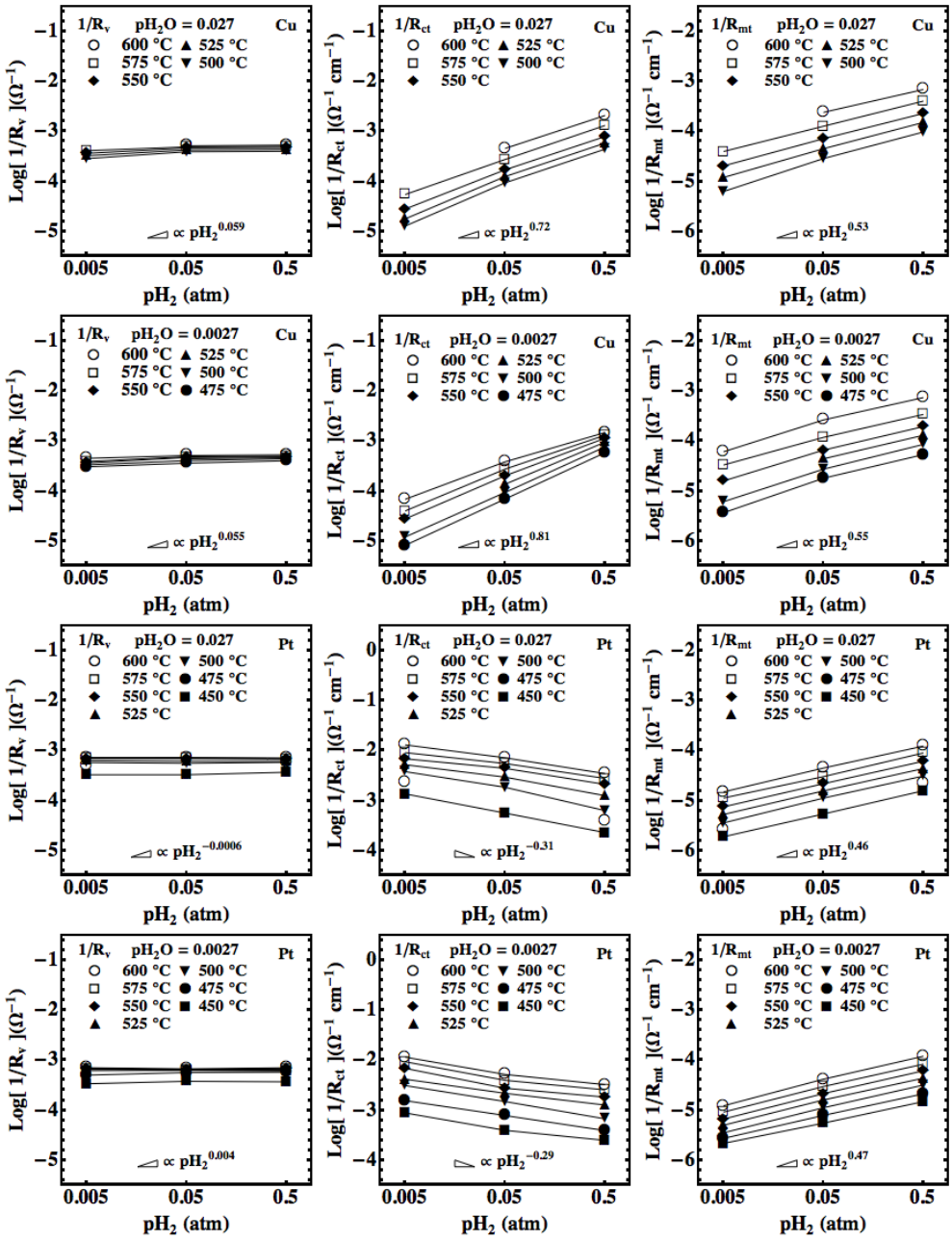

Figure 7: Cu (*top*) and Pt (*bottom*) point-contact electrode conductance: Electrolyte volume (*left*), charge transfer (*middle*), and mass transfer (*right*), plotted as Log(1/R) vs. Log(pH_2) for pH_2O = 0.027 (*above*) and pH_2O = 0.0027 (*below*).

The charge transfer resistance makes up the most significant difference between the two electrode materials. For Cu, the charge transfer conductance, $1/R_{ct}$, exhibits a $pH_2^{3/4}$ dependence, while for Pt, $1/R_{ct}$ exhibits a $pH_2^{-1/4}$ dependence. The mass transfer conductance, $1/R_{mt}$, exhibits a $pH_2^{1/2}$ dependence for both metal electrode materials.

3.4. pH_2O dependencies

The data shown in Fig. 7 was plotted vs. pH_2O, and selected graphs are shown in Fig. 8.

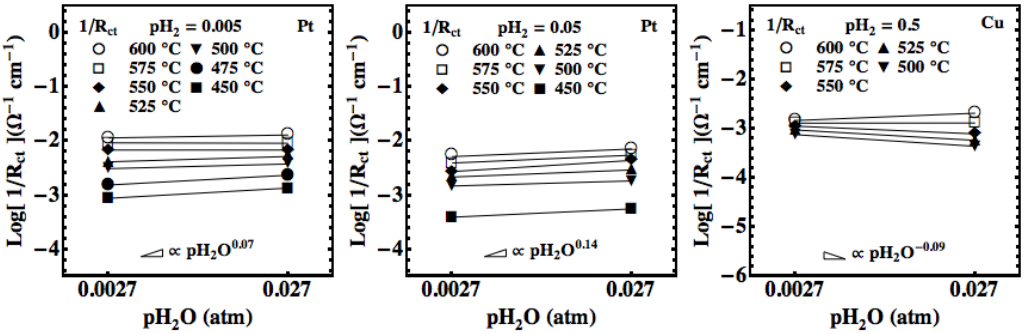

Figure 8: Selected charge transfer conductances, plotted as Log($1/R$) vs. Log(pH_2O) for Pt at pH_2 = 0.005 and 0.05 (*left*), and Cu at pH_2 = 0.5 (*right*).

The Cu point-contact electrode has a slight pH_2O dependence of the charge transfer resistance at pH_2 = 0.5, but the pH_2O dependence of the charge transfer conductance is negligible at pH_2 = 0.05 and 0.005 (not shown). The pH_2O dependencies of the mass transfer conductance is negligible for all measured hydrogen pressures and are also not shown.

The Pt point-contact electrode shows a slight pH_2O dependence at lower hydrogen concentrations, with the effects being more pronounced at low temperature. At pH_2 = 0.5 the pH_2O dependence of the charge transfer conductance is negligible, as is the pH_2O dependence of the mass transfer conductance for all hydrogen pressures and temperatures (not shown). The average pH_2O dependence is given at the bottom of each of the plots shown in Fig. 8.

3.5. Temperature dependencies

The temperature dependencies of $1/R_{ct}$ and $1/R_{mt}$ for Cu and Pt are shown in Fig. 9.

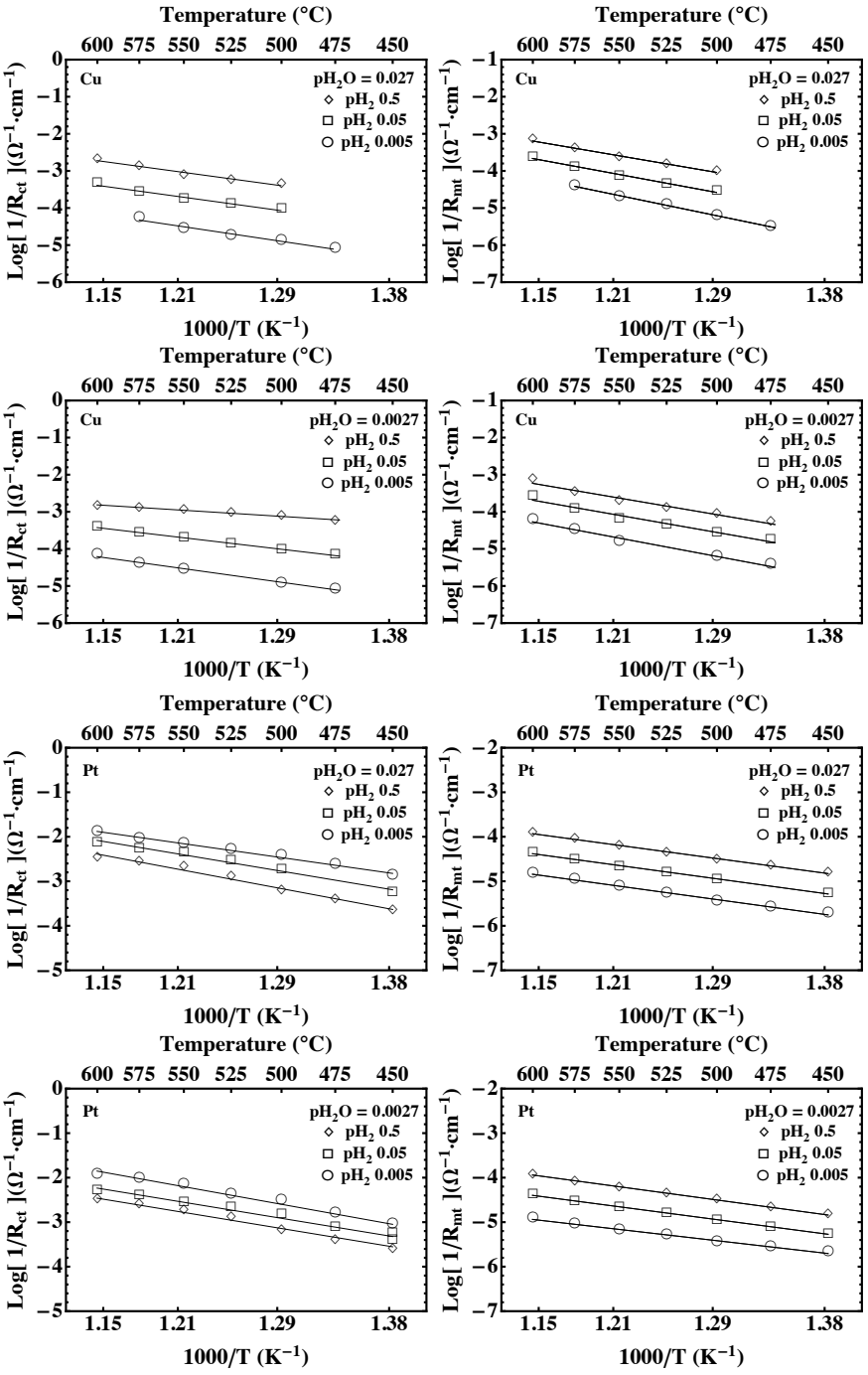

Figure 9: Plots of $\mathrm{Log}(1/R_i)$ vs. $1000/T$ for charge transfer (*left*) and mass transfer (*right*) for the Cu (*top*) and Pt (*bottom*) point contact electrodes at pH_2O = 0.027 and 0.0027.

The conductance in the studied temperature range can, to a first approximation, be expressed as,

$$\frac{1}{R} = A_0 \left(pH_2\right)^n \left(pH_2O\right)^m \mathbf{e}^{-\frac{\Delta H}{k_b T}} \tag{2}$$

where n and m are the pH_2 and pH_2O dependencies, respectively. ΔH is the activation enthalpy and k_b is the Boltzmann constant. Log-linear regressions of (2) were performed on the plots in Fig. 9, and the activation enthalpies were extracted. Table 2 reports the means and standard deviations of the pre-exponential A_0, n and m from Sections 3.3 and 3.4, respectively, as well as the activation enthalpy, ΔH.

Table 2: Mean and standard deviations ($\overline{x_i} \pm \sigma_i$) of the hydrogen ($n_i$) and water vapor ($m_i$) pressure dependencies as obtained from Sections 3.3 and 3.4 for charge transfer (ct) and mass transfer (mt), the activation enthalpies (ΔH_i), as well as the derived pre-exponentials, Log($A_{0,i}$), for each of the Cu and Pt point-contact electrodes.

$\overline{x_i} \pm \sigma_i$	Cu	Pt
n_{ct}	0.77 ± 0.09	-0.30 ± 0.04
m_{ct}	-0.02 ± 0.12	0.08 ± 0.08
ΔH_{ct} (eV)	0.82 ± 0.21	0.93 ± 0.09
Log($A_{0,ct}(\Omega^{-1}cm^{-1})$)	2.21 ± 0.10	3.00 ± 0.06
n_{mt}	0.53 ± 0.04	0.46 ± 0.02
m_{mt}	0.04 ± 0.04	0.01 ± 0.03
ΔH_d (eV)	1.21 ± 0.09	0.73 ± 0.05
Log($A_{0,mt}(\Omega^{-1}cm^{-1})$)	4.00 ± 0.13	0.42 ± 0.04

Pre-exponentials depend significantly upon geometric factors, concentrations of species and vibrational attempt rates. The difference in the charge transfer pre-exponential of approximately 160 $\Omega^{-1}cm^{-1}$ for Cu, compared to 1000 $\Omega^{-1}cm^{-1}$ for Pt, indicates that Cu has fewer available sites for charge transfer to take place. However, the activation enthalpy for charge transfer is lower for Cu than for Pt, indicating the reaction takes place more readily on Cu. Charge transfer reactions on Cu have been reported to have different activation enthalpies for different surface orientations, from approximately 0.5 to 1 eV [37, 47–49]. This variation is possibly due to competitive adsorption of H_2 and O_2 vs. H_2O at preferential sites, though this could also be due to the diffusion of hydrogen through the bulk copper lattice at high

pH_2. Hydrogen has been previously reported to accumulate just below the surface of Cu and Cu-based metal alloys, forming small hydrogen bubbles [39, 50]. Indications of this were also obtained in this study, as seen in Fig. 10, though it is unknown to what extent this contributed to the measured resistance of the Cu-BZCY27 interface.

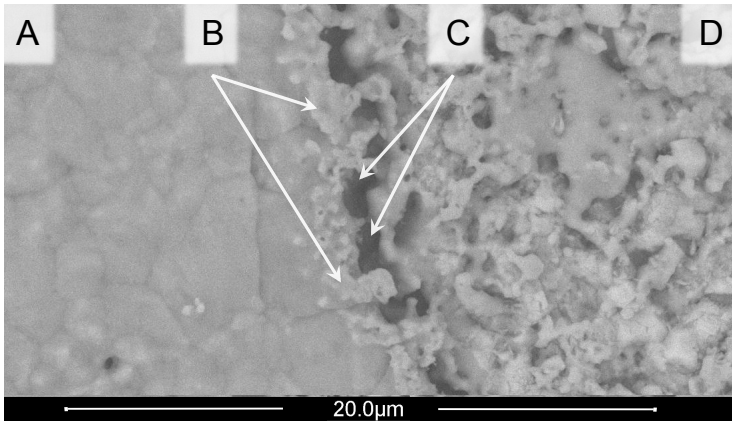

Figure 10: Post-testing SEM image of the Cu point-contact electrode which on the left shows: A) the grains of the metal surface, with B) the 3pb interface. To the right of the 3pb interface shows: C) vacant areas under the surface of the metal, and D) the irregular 2pb metal-electrolyte interface where hydrogen bubbles may have also formed.

In a recent DFT study of the Pd-BZY 3pb interface [51] the activation energy for the proton transfer step of the charge transfer reaction was calculated to be near 1 eV, independent of the type of metal electrode used, which is in reasonable agreement with the experimental results for both Cu and Pt, as obtained in this study.

The pre-exponential for mass transfer for Cu is almost 4000 times greater than that of Pt, approximately 10000 vs. 2.6 $\Omega^{-1}cm^{-1}$, respectively. The higher activation enthalpy for mass transfer on Cu combines that of hydrogen adsorption, dissociation and surface diffusion, and is within literature values of approximately 1.1 to 1.4 eV [37, 48, 52–55]. Hydrogen dissociation on Pt surfaces is reported to be nearly non-activated, and the activation enthalpies obtained here are those of hydrogen adsorption, in agreement with literature reports of approximately 0.65 to 0.76 eV [37, 56–61]. For Cu, the combination of a higher pre-exponential and activation enthalpy indicates that mass transfer processes are less favorable and use more of the Cu metal

surface adjacent to the 3pb for adsorption and dissociation to occur. With a lower pre-exponential and activation enthalpy, mass transfer on Pt is much more favorable, and thus needs less area to complete the process.

4. Discussion

4.1. Hydrogen oxidation reaction model and pH_2 dependencies

An HOR model was developed to explain the characteristics of the data presented in previous sections. Langmuir adsorption theory and Butler-Volmer charge transfer formalism have previously been used to describe electrochemical redox processes on solid-state oxide electrolytes [62, 63]. Here, it is assumed that associative adsorption will be predominant, such as the case for Cu, and occur first. However, on Pt, dissociative adsorption is more favorable. Using Langmuir theory, associative and dissociative adsorption are often lumped together, and along with diffusion, are commonly used to describe mass transfer as a single process.

H_2 Oxidation Half-Cell Model:

$$\text{1 - adsorption: } H_2(g) + v_{ads} \leftrightarrow H_{2,ads} \tag{3}$$

$$\underline{\text{2 - dissociation: } H_{2,ads} + v_{ads} \leftrightarrow 2H_{ads}} \tag{4}$$

$$\text{3a - surface diffusion: } H_{ads} + v_{3pb} \leftrightarrow H_{3pb} + v_{ads} \tag{5}$$

$$\text{3b - } \begin{cases} \text{dissolution into metal: } H_{ads} + v_i \leftrightarrow H_i^x + v_{ads} \\ \text{interstitial diffusion: } H_i^x + v_{2pb} \leftrightarrow H_{2pb} + v_i \end{cases} \tag{6}$$

$$\text{4 - charge transfer: } H_{pb} + O_O^{2-} \leftrightarrow OH_O^- + e^- + v_{pb} \tag{7}$$

After adsorption onto a vacant surface site, v_{ads}, and the subsequent dissociation, H transports to the phase boundary (pb). This may happen via two paths, on the metal surface to the 3pb, or via dissolution into and interstitially through the bulk metal to the 2pb. Charge transfer then takes place at the pb, with proton transfer to an available oxygen ion in the electrolyte, and electron transfer to the metal. Using Langmuir adsorption theory to describe mass transfer processes, and Butler-Volmer formalism for charge transfer, the rate equations according to the proposed HOR model are,

$$r_1 = k_1^+ pH_2 \left(1 - \Theta_{ads}\right) - k_1^- \Theta_{ads}^{H_2} \tag{8}$$

$$r_2 = k_2^+ \Theta_{ads}^{H_2} (1 - \Theta_{ads}) - k_2^- (\Theta_{ads}^H)^2 \tag{9}$$

$$r_{3s} = k_{surf.}^+ \Theta_{ads}^H (1 - \Theta_{3pb}) - k_{surf.}^- \Theta_{3pb}^H (1 - \Theta_{ads}) \tag{10}$$

$$r_{3i} = \begin{cases} k_{diss.}^+ \Theta_{ads}^H (1 - \Theta_i) - k_{diss.}^- \Theta_i^H (1 - \Theta_{ads}) \\ k_{diff.}^+ \Theta_i^H (1 - \Theta_{2pb}) - k_{diff.}^- \Theta_{2pb}^H (1 - \Theta_i) \end{cases} \tag{11}$$

$$r_4 = k_4^+ \Theta_{pb}^H [O_O^{2-}] \, exp^{\beta\zeta(E-E_0)} - k_4^- [OH_O^-] (1 - \Theta_{pb}) \, exp^{-(1-\beta)\zeta(E-E_0)} \tag{12}$$

The terms k^+ and k^- are the forward and backward rate constants, respectively. The symbol Θ denotes site fraction and is equivalent to the activity of H; the superscript indicates the H species, and the subscripts ads, i, $2pb$ and $3pb$ indicate location as "adsorbed", "interstitial", "two-phase boundary" and "three-phase boundary", respectively. In r_3, the k subscript *surf.* is for surface, *diss.* for dissolution and *diff.* for diffusion. $(1-\Theta)$ then represents the activity of the vacant sites. $[O_O^{2-}]$ and $[OH_O^-]$ are the concentrations of oxide ions and protons in the electrolyte, respectively. From the Butler-Volmer equation, the symmetry coefficient for electron transfer is commonly assumed to be, $\beta = 1/2$. $\zeta = F/RT$ where F is Faraday's constant , R is the universal gas constant, T is temperature. E is the cell potential and E_0 is the standard potential.

(8) describes the rate of physisorption of H_2 onto the metal surface. (9) describes the rate of dissociation and chemisorption of atomic hydrogen. (10) describes the rate of diffusion of atomic hydrogen, H_{ads}, across the metal surface to the 3pb. (11) describes the rate of dissolution and interstitial diffusion of atomic hydrogen through the bulk metal to the 2pb. (12) describes the rate of charge transfer, where pb (phase-boundary) denotes both the 2pb and 3pb. In the following treatment we will, for simplicity, assume that the surface process is predominant.

At thermodynamic equilibrium the net rate is 0, and from (8-11) with the mass transfer rate constant $\mathbf{K}_{mt} = \sqrt{(k_1^+/k_1^-)\,(k_2^+/k_2^-)}(k_3^+/k_3^-)$, the surface coverage of chemisorbed H at the phase boundary is,

$$\Theta_{pb}^H = \mathbf{K}_{mt} \, pH_2^{1/2} (1 - \Theta_{pb}) \tag{13}$$

(13) is then converted into current through the relation, $i = -nF\, r_{lim} = i_{anodic} - i_{cathodic}$, where r_{lim} is the rate limiting step. In equilibrium, the net

current, $i = 0$, and the exchange current density, i_0, follows,

$$i_0 = i_{0,+} = i_{0,-} \tag{14}$$

where $i_{0,+} = i_{0,anodic}$ and $i_{0,-} = i_{0,cathodic}$. At open circuit, the exchange current density is inversely proportional to measured resistance through Ohm's law, $v = iR$. With the low coverage assumption, $(1-\Theta_{pb}) = 1$, the pH_2 dependence of the mass transfer rate limiting case is,

$$i_{0,\,mt} \propto \frac{1}{R_{mt}} \propto pH_2^{1/2} \tag{15}$$

Eq. (15) reflects the hydrogen pressure dependence of adsorption, dissociation and subsequent transport to the pb, and describes the experimentally observed pH_2 dependence of mass transfer for both metals.

Next, consider rate equation (12) of the H_2 oxidation half-cell model. With the definition of electrochemical potential as,

$$\tilde{\mu}_i = \mu_i^0 + RT\ln(\chi_i) + zF\phi_i$$

where μ_i^0 is the standard chemical potential, χ is activity, z is charge and ϕ_i is the electric potential of species i. Similar to other derivations of the hydrogen electrode potential [64, 65], (12) then becomes,

$$\begin{aligned} &\mu^0_{\Theta^H_{pb}} + RT\ln(\Theta^H_{pb}) + \mu^0_{O^{2-}_O} + RT\ln([O^{2-}_O]) = \\ &\qquad \mu^0_{OH^-_O} + RT\ln([OH^-_O]) + F\phi_{OH^-_O} + \mu^0_{e^-} - F\phi_{e^-} + RT\ln(1-\Theta_{pb}) \end{aligned} \tag{16}$$

with the changes in the cell and standard potentials as,

$$\Delta\phi = \phi_{e^-} - \phi_{OH^-_O} \qquad \text{and} \qquad \Delta\phi^0 = \frac{-\mu^0_{\Theta^H_{pb}} - \mu^0_{O^{2-}_O} + \mu^0_{OH^-_O} + \mu^0_{e^-}}{F} \tag{17}$$

finally yielding the half cell potential of the hydrogen electrode,

$$\Delta\phi - \Delta\phi^0 = E_{eq} - E^0 = \frac{1}{\zeta}\ln\left(\frac{[OH^-_O](1-\Theta_{pb})}{\Theta^H_{pb}[O^{2-}_O]}\right) \tag{18}$$

By defining the concentrations of products, $C_P = [OH^-_O](1-\Theta_{pb})$, and reactants, $C_R = \Theta^H_{pb}[O^{2-}_O]$. Then inserting (18) into (12) where at equilibrium the cell potential $E = E_{eq}$.

$$r_{4,eq} = k_4^0\, C_R\, exp^{\beta\zeta(\frac{1}{\zeta}\ln\left(\frac{C_P}{C_R}\right))} = k_4^0\, C_P\, exp^{-(1-\beta)\zeta(\frac{1}{\zeta}\ln\left(\frac{C_P}{C_R}\right))} \tag{19}$$

Again using $i = -nFr$ with $n = 1$, the exchange current density is now defined in terms of both reactants and products,

$$i_0 = F k_4^0 \, C_R^{(1-\beta)} \, C_P^{\beta} \tag{20}$$

It is reasonable to assume that in a fully hydrated and protonated electrolyte, $[OH_O^-]$ is constant, and that the concentration of oxygen ions in the perovskite structure ABO_3 is approximately equal to unity, $[O_O^{2-}] \cong 1$. After simplification with C_P, C_R, (13) and the heterogeneous rate constant, $\mathbf{K}_h^0 = k_4^0 \mathbf{K}_{mt}$,

$$i_{0,r_4} = F \, \mathbf{K}_h^0 \, pH_2^{\frac{(1-\beta)}{2}} (1 - \Theta_{pb}) \tag{21}$$

or more significantly,

$$i_{0,ct} \propto \frac{1}{R_{ct}} \propto pH_2^{\frac{(1-\beta)}{2}} (1 - \Theta_{pb}) \tag{22}$$

The charge transfer conductance, $1/R_{ct}$, then scales as the product of the pH_2 dependence obtained from mass transfer, the charge transfer symmetry coefficient and the activity of vacant sites at the pb.

Pt dissociatively adsorbs hydrogen, which may then segregate at the terminations of surfaces [66]. This will yield high coverage at corners and edges, such as the 3pb. By using the Langmuir isotherm describing high coverage with dissociative adsorption as $(1 - \Theta_{3pb}) = pH_2^{-1/2}$ in (21),

$$i_{0,ct} \propto \frac{1}{R_{ct}} \propto pH_2^{-1/4} \tag{23}$$

Then the $pH_2^{-1/4}$ charge transfer hydrogen pressure dependence describing the experimental results for Pt is obtained directly.

Cu is not known to have high surface coverage of hydrogen [67, 68]. In the low pO_2 of the H_2–H_2O atmospheres used, Cu does not form the a stable Cu_2O phase, however, it is proposed that most of the active sites at the 3pb are occupied by adsorbed oxygen. This causes an additional step in the charge transfer reaction. At the 3pb, H_{ads} will first reduce the oxygen at a 3pb site in order to become the H_{3pb} species,

$$3H_{ads} + O_{3pb} \leftrightarrow H_{3pb} + H_2O(g) + 3v_{ads} \tag{24}$$

The rate equation associated with (24) is,

$$r = k^+ \, (\Theta_{ads}^H)^3 \, \Theta_{3pb}^O \; - \; k^- \, \Theta_{3pb}^H \, pH_2O \, (1 - \Theta_{ads})^3 \tag{25}$$

Which then yields the H_{3pb} coverage as,

$$\Theta^{H}_{3pb} = \mathbf{K}_{mt}\, pH_2^{3/2} \frac{\Theta^{O}_{3pb}}{pH_2O}(1 - \Theta_{3pb}) \tag{26}$$

and with a constant proportional pH_2O and Θ^{O}_{3pb}, yields the exchange current density as,

$$i_{0,r_5} = F\, \mathbf{K}^{0}_{h}\, pH_2^{\frac{3(1-\beta)}{2}} (1 - \Theta_{3pb}) \tag{27}$$

Again with $\beta = 0.5$, and the low coverage of $(1 - \Theta_{3pb}) = 1$,

$$i_{0,ct} \propto \frac{1}{R_{ct}} \propto pH_2^{3/4} \tag{28}$$

Then the $pH_2^{3/4}$ hydrogen pressure dependence is obtained, which describes the experimental results herein.

In this section pH_2 dependencies and hypotheses have been presented that describe the mass transfer and charge transfer data obtained in this metal point-contact electrode study. The mass transfer processes of hydrogen adsorption and dissociation, emphasizing low coverage for both Cu and Pt, display a $pH_2^{1/2}$ dependency. The pH_2 dependencies derived for charge transfer are influenced by the symmetry coefficient, β, and by the coverage of atomic hydrogen at the 3pb, H_{3pb}, which may differ significantly from the overall surface coverage of the metal. First, for Pt, with high 3pb coverage, a $pH_2^{-1/4}$ dependence was derived. Second, for Cu, with the hypothesis of adsorbed oxygen at active 3pb sites due to the water-vapor containing atmosphere, and a low hydrogen coverage assumption, the $pH_2^{3/4}$ dependence was obtained.

5. Conclusions

The reaction kinetics of Pt and Cu point-contact electrodes on a BZCY72 electrolyte were studied over a range of temperatures and hydrogen pressures using impedance spectroscopy. The charge transfer hydrogen pressure dependencies were $pH_2^{3/4}$ for Cu, attributed to a high occupancy of adsorbed oxygen at three-phase boundary sites in the water-vapor containing atmosphere, and $pH_2^{-1/4}$ for Pt, corresponding to a hydrogen saturated interface.

The activation enthalpies for charge transfer are similar for both metals, 0.82 eV for Cu, and 0.93 eV for Pt. Cu and Pt exhibit pre-exponentials of 160 $\Omega^{-1}cm^{-1}$ vs. 1000 $\Omega^{-1}cm^{-1}$, respectively. Mass transfer exhibited a $pH_2^{1/2}$ dependency for both metals. The activation enthalpy for mass transfer is higher for Cu than Pt, $1.21\,eV$ vs. $0.73\,eV$, respectively, reflecting that mass transfer is a slower process on Cu. The pre-exponentials for mass transfer of approximately 10000 $\Omega^{-1}cm^{-1}$ for Cu and 2.6 $\Omega^{-1}cm^{-1}$ for Pt, also indicate that for Cu, this process likely takes place on a larger geometric area adjacent to the 3pb than the same process on Pt. It is concluded from this work that although Cu is a suitable candidate electrode material for hydrocarbon applications due to it's resistance to carbon deposition, pure Cu suffers from poor catalytic activity for the hydrogen oxidation reaction. In order to perform efficiently, it is suggested that Cu will benefit from modifications via alloying, or through the addition of another phase catalytically active towards hydrogen dissociation.

Acknowledgements

The authors gratefully acknowledge financial support from the Research Council of Norway through the program NANO2021, RoMA, project number 219194. We also thank Drs. Nahum M. Carcases, Ragnar Strandbakke, Einar Vøllestad, and Min Chen for valuable contributions.

References

1. H. Iwahara, T. Esaka, H. Uchida, N. Maeda . "Proton conduction in sintered oxides and its application to steam electrolysis for hydrogen production". *Solid State Ionics* 1981;**3/4**:359–363.

2. H. Iwahara, H. Uchida, S. Tanaka . "High temperature type proton conductor based on $SrCeO_3$ and its application to solid electrolyte fuel cells". *Solid State Ionics* 1983;**9-10**:1021 – 1026.

3. H. Iwahara . "Proton conducting ceramics and their applications". *Solid State Ionics* 1996;**86-88**:9–15.

4. Kreuer, K. D. . "Proton-conducting oxides". *Annual Review of Materials Research* 2003;**33**(1):333 – 359.

5. Y. Larring, T. Norby . "Protons in rare earth oxides". *Solid State Ionics* 1995;**77**:147 – 151.

6. Y. Larring, T. Norby . "The equilibrium between water vapour, protons, and oxygen vacancies in rare earth oxides". *Solid State Ionics* 1997; **97**(1-4):523 – 528.

7. K.D. Kreuer . "Aspects of the formation and mobility of protonic charge carriers and the stability of perovskite-type oxides". *Solid State Ionics* 1999;**125**(1-4):285 – 302.

8. Bonanos N. "Oxide-based protonic conductors: point defects and transport properties". *Solid State Ionics* 2001;**145**:265 – 274.

9. J. Li, J.L. Luo, K.T. Chuang, A.R. Sanger . "Chemical stability of Y-doped $Ba(Ce,Zr)O_3$ perovskites in H_2S-containing H_2". *Electrochimica Acta* 2008;**53**(10):3701 – 3707.

10. Kang L. *"Ceramic Membranes for Separation and Reaction"*. ISBN 978-0-470-01440. England: John Wiley & Sons Ltd; 2007.

11. S. Ricote, G. Caboche, O. Heintz . "Synthesis and proton incorporation in $BaCe_{0.9-x}Zr_xY_{0.1}O_{3-\delta}$". *Journal of Applied Electrochemistry* 2009; **39**:553–557.

12. S. Ricote, N. Bonanos, G. Caboche . "Water vapour solubility and conductivity study of the proton conductor $BaCe_{0.9-x}Zr_xY_{0.1}O_{3-\delta}$". *Solid State Ionics* 2009;**180**(14–16):990 – 997.

13. S. Ricote, N. Bonanos, M.C. Marco de Lucas, G. Caboche . "Structural and conductivity study of the proton conductor $BaCe_{0.9-x}Zr_xY_{0.1}O_{3-\delta}$ at intermediate temperatures". *Journal of Power Sources* 2009;**193**:189–193.

14. Y. Lin, R. Ran, Y. Guo, W. Zhou, R. Cai, J. Wang, Z. Shao . "Proton-conducting fuel cells operating on hydrogen, ammonia and hydrazine at intermediate temperatures". *International Journal of Hydrogen Energy* 2010;**35**(7):2637 – 2642.

15. E. Fabbri, L. Bi, H. Tanaka, D. Pergolesi, E. Traversa . "Chemically Stable Pr and Y Co-Doped Barium Zirconate Electrolytes with High Proton Conductivity for Intermediate-Temperature Solid Oxide Fuel Cells". *Advanced Functional Materials* 2011;**21**:158–166.

16. K. Ryu, S. Haile . "Chemical stability and proton conductivity of doped $BaCeO_3$ - $BaZrO_3$ solid solutions. *Solid State Ionics* 1999;**125**:355 – 367.

17. E. Fabbri, A. D'Epifanio, E. Di Bartolomeo, S. Licoccia, E. Traversa . "Tailoring the chemical stability of $BaCe_{0.8-x}Zr_xY_{0.2}O_{3-\delta}$ protonic conductors for Intermediate Temperature Solid Oxide Fuel Cells (IT-SOFCs). *Solid State Ionics* 2008;**179**(15–16):558 – 564.

18. M.D. Gross, J.M. Vohs, R.J. Gorte . "A study of thermal stability and methane tolerance of Cu-based SOFC anodes with electrodeposited Co". *Electrochimica Acta* 2007;**52**(5):1951 – 1957.

19. S.W. Jung, J.M. Vohs, R.J. Gorte . "Preparation of SOFC Anodes sby Electrodeposition". *Journal of The Electrochemical Society* 2007; **154**(12):B1270–B1275.

20. O. Costa-Nunes, R.J. Gorte, J.M. Vohs . "Comparison of the performance of Cu-CeO_2-YSZ and Ni-YSZ composite SOFC anodes with H_2, CO, and syngas". *Journal of Power Sources* 2005;**141**:241–245.

21. V.K. Venkatesan, S. McIntosh, R.J. Gorte, J.M. Vohs . "Measurement of electrode overpotentials for direct hydrocarbon conversion fuel cells. *Solid State Ionics* 2004;**166**(1 - 2):191 – 197.

22. S. Park, J.M. Vohs, R.J. Gorte . "Direct oxidation of hydrocarbons in a solid-oxide fuel cell". *Nature* 2000;**404**(6775):265–267.

23. R.J. Gorte, S. Park, J.M. Vohs, C. Wang . "Anodes for Direct Oxidation of Dry Hydrocarbons in a Solid-Oxide Fuel Cell. *Advanced Materials* 2000;**12**(19):1465–1469.

24. R.J. Gorte, J.M. Vohs, S. McIntosh . "Recent developments on anodes for direct fuel utilization in SOFC". *Solid State Ionics* 2004;**175**(1 - 4):1 – 6.

25. S.J. Gentry, J.G. Firth, A. Jones . "Catalytic oxidation of hydrogen over platinum". *J Chem Soc, Faraday Trans 1* 1974;**70**:600–604.

26. Jiang, S. P. and Badwal, S. P. S. . "Hydrogen Oxidation at the Nickel and Platinum Electrodes on YttriaTetragonal Zirconia Electrolyte". *Journal of The Electrochemical Society* 1997;**144**(11):3777 – 3784.

27. D. Kek, N. Bonanos . "Investigation of hydrogen oxidation reaction on a metal/perovskite proton conductor interface by impedance spectroscopy". *Vacuum* 2001;**61**:453 – 457.

28. D. Kek, N. Bonanos, M. Mogensen, S. Pejovnik . "Effect of electrode material on the oxidation of H_2 at the metal - $Sr_{0.995}Ce_{0.95}Y_{0.05}O_{2.970}$ interface". *Solid State Ionics* 2000;**131**:249 – 259.

29. T. Horita, N. Sakai, H. Yokokawa, M. Dokiya, T. Kawada . "Characterization of ceria coated YSZ by a platinum point electrode in H_2-H_2O atmosphere". *Solid State Ionics* 1996;**86 - 88, Part 2**:1259 – 1266.

30. T. Jacobsen, B. Zachau-Christiansen, L. Bay, M.J. Jørgensen . "Hysteresis in the solid oxide fuel cell cathode reaction". *Electrochimica Acta* 2001;**46**(7):1019 – 1024.

31. F. Mauvy, C. Lalanne, S. Fourcade, J.M. Bassat, J.C. Grenier . "Impedance spectroscopy study of $Nd_2NiO_{4+\delta}$, LSM and platinum electrodes by micro-contact technique". *Journal of the European Ceramic Society* 2007;**27**(13 - 15):3731 – 3734.

32. T. Horita, H. Kishimoto, K. Yamaji, Y. Xiong, N. Sakai, M.E. Brito, H. Yokokawa . "Materials and reaction mechanisms at anode/electrolyte interfaces for SOFCs". *Solid State Ionics* 2006;**177**(19 - 25):1941 – 1948.

33. W.G. Bessler, M. Vogler, H. Stormer, D. Gerthsen, A. Utz, A. Weber, E. Ivers-Tiffee . "Model anodes and anode models for understanding the mechanism of hydrogen oxidation in solid oxide fuel cells". *Phys Chem Chem Phys* 2010;**12**:13888–13903.

34. M. Mogensen, S. Skaarup . "Kinetic and geometric aspects of solid oxide fuel cell electrodes". *Solid State Ionics* 1996;**86–88**:1151 – 1160.

35. E.J.L. Schouler, M. Kleitz . "Electrocatalysis and Inductive Effects at the Gas, Pt/Stabilized Zirconia Interface". *Journal of The Electrochemical Society* 1987;**134**(5):1045–1050.

36. B. Hammer, J.K. Nørskov . "Theoretical surface science and catalysis—calculations and concepts". In: B.C. Gates, H. Knozinger , editor. *Impact of Surface Science on Catalysis*; vol. 45 of *Advances in Catalysis*. Academic Press; 2000, p. 71–129.

37. P.B. Rasmussen, P.M. Holmblad, H. Christoffersen, P.A. Taylor, I. Chorkendorff . "Dissociative adsorption of hydrogen on Cu(100) at low temperatures". *Surface Science* 1993;**287-288, Part 1**(0):79 – 83.

38. T. Ishikawa R.B. McLellan . "The diffusivity of hydrogen in copper at low temperatures". *Journal of Physics and Chemistry of Solids* 1985; **46**(4):445 – 447.

39. H.B. Zhou, Y.Zhang, X. Ou . "Dissolution and diffusion behaviors of hydrogen in copper: A first-principles investigation". *Computational Materials Science* 2013;**79**:923 – 928.

40. H. Horinouchi, M. Shinohara, T. Otsuka, K. Hashizume, T. Tanabe . "Determination of hydrogen diffusion and permeation coefficients in pure copper at near room temperature by means of tritium tracer techniques. *Journal of Alloys and Compounds* 2013;**580, Supplement 1**:S73 – S75.

41. P. Babilo, S.M. Haile . "Enhanced Sintering of Yttrium-Doped Barium Zirconate by Addition of ZnO". *Journal of the American Ceramic Society* 2005;**88**(9):2362–2368.

505 42. S. Nikodemski, J. Tong, R. O'Hayre . "Solid-state reactive sintering
506 mechanism for proton conducting ceramics". *Solid State Ionics* 2013;
507 **253**(0):201 – 210.

508 43. S. Ricote, G. Caboche, C. Estournes, N. Bonanos . "Synthesis, Sin-
509 tering, and Electrical Properties of $BaCe_{0.9x}Zr_xY_{0.1}O_{3-\delta}$". *Journal of*
510 *Nanomaterials* 2008;**2008**:1–6.

511 44. Y. Yamazaki, R. Hernandez-Sanchez, S. M. Haile . "High Total Pro-
512 ton Conductivity in Large-Grained Yttrium-Doped Barium Zirconate.
513 *Chemistry of Materials* 2009;**21**(13):2755–2762.

514 45. J.H. Hwang, K.S. Kirkpatrick, T.O. Mason, E.J. Garboczi . "Experi-
515 mental limitations in impedance spectroscopy:: Part IV. Electrode con-
516 tact effects". *Solid State Ionics* 1997;**98**(1-2):93 – 104.

517 46. J.T.S. Irvine, D.C. Sinclair, A.R. West . "Electroceramics: Characteri-
518 zation by Impedance Spectroscopy. *Advanced Materials* 1990;**2**(3):132–
519 138.

520 47. M.F. Luo, D.A. MacLaren, I.G. Shuttleworth, W. Allison . "Preferen-
521 tial sub-surface occupation of atomic hydrogen on Cu(111)". *Chemical*
522 *Physics Letters* 2003;**381**(5–6):654 – 659.

523 48. J. Strömquist, L. Bengtsson, M. Persson, B. Hammer" . "The dynamics
524 of H absorption in and adsorption on Cu(111). *Surface Science* 1998;
525 **397**(1–3):382 – 394.

526 49. M.F. Luo, D.A. MacLaren, W. Allison . "Migration and abstraction of
527 H-atoms from the Cu(111) surface". *Surface Science* 2005;**586**(1-3):109–
528 114.

529 50. Å. Martinsson, R. Sandström . "Hydrogen depth profile in phosphorus-
530 doped, oxygen-free copper after cathodic charging". *Journal of Materials*
531 *Science* 2012;**47**(19):6768–6776.

532 51. M. Malagoli, M. L. Liu, H. C. Park, A. Bongiorno . "Protons crossing
533 triple phase boundaries based on a metal catalyst, Pd or Ni, and barium
534 zirconate. *Phys Chem Chem Phys* 2013;**15**:12525–12529.

52. P.K. Johansson . "Chemisorption of molecular hydrogen on simple metal surfaces". *Surface Science* 1981;**104**(2):510 – 526.

53. D.J. Auerbach, C.T. Rettner, H.A. Michelsen . "Interaction dynamics of hydrogen at a Cu(111) surface". *Surface Science* 1993;**283**(1–3):1 – 8.

54. B.E. Hayden, C.L.A. Lamont . "Coupled translational-vibrational activation in dissociative hydrogen adsorption on Cu(110)". *Phys Rev Lett* 1989;**63**:1823–1825.

55. R.C. Mowrey, G.J. Kroes, G. Wiesenekker, E.J. Baerends . "Dissociative adsorption of H2 on Cu(100): A four-dimensional study of the effect of rotational motion on the reaction dynamics". *The Journal of Chemical Physics* 1997;**106**(10):4248–4259.

56. R. Lewis, R. Gomer . Adsorption of hydrogen on platinum. *Surface Science* 1969;**17**(2):333 – 345.

57. W.T Lee, L. Ford, P. Blowers, H.L. Nigg, R.I. Masel . "Why do heats of adsorption of simple gases on platinum surfaces vary so little with surface structure?". *Surface Science* 1998;**416**(1–2):141 – 151.

58. B. Klötzer, E. Bechtold . "Hydrogen adsorption and the transformation of the Pt(100) surface structure". *Surface Science* 1993;**295**(3):374 – 384.

59. P.R. Norton, P.J. Richards . "The heat of adsorption of hydrogen on platinum". *Surface Science* 1974;**44**(1):129 – 140.

60. W.H. Weinberg, R.P. Merrill . "Crystal field surface orbital - Bond-energy bond-order (CFSO-BEBO) model for chemisorption: Application to hydrogen adsorption on a platinum (111) surface". *Surface Science* 1972;**33**(3):493 – 515.

61. J. Andzelm . "Molecular orbital study of the chemisorption of hydrogen on platinum surfaces. *Surface Science* 1981;**108**(3):561 – 577.

62. J.D. Kim, G.D. Kim, J.W. Moon, Y.l. Park, W.H. Lee, K. Kobayashi, M. Nagai, C.E. Kim . "Characterization of LSM-YSZ composite electrode by ac impedance spectroscopy". *Solid State Ionics* 2001;**143**(3-4):379 – 389.

567 63. T. Hosoi, T. Yonekura, K. Sunada, K. Sasaki . "Exchange Current
568 Density of SOFC Electrodes: Theoretical Relations and Partial Pressure
569 Dependencies Rate-Determined by Electrochemical Reactions". *Journal*
570 *of The Electrochemical Society* 2015;**162**(1):F136 – F152.

571 64. H. Gerischer . *"The CRC Handbook of Solid State Electrochemistry"*.
572 CRC Press; 1997.

573 65. R. O'Hayre, S.W. Cha, W. Colella, F.B. Prinz . *"Fuel Cell Fundamen-*
574 *tals"*. Wiley; 2 ed.; 2009.

575 66. A. Pundt, R. Kirchheim . Hydrogen in metals: Microstructural aspects.
576 *Annual Review of Materials Research* 2006;**36**(1):555–608.

577 67. P. Sandl, U. Bischler, E. Bertel . "The interaction of atomic hydrogen
578 with Cu(110). *Surface Science* 1993;**291**(1):29 – 38.

579 68. D.R. Rossington, S.J. Holden . "Equilibrium Coverage of Copper by
580 Chemisorbed Hydrogen". *Nature* 1963;**199**(4893):589–589.